

Efficient Spin Transfer in $\text{WTe}_2/\text{Fe}_3\text{GeTe}_2$ van der Waals Heterostructure Enabled by Direct Interlayer p-Orbital Hybridization

H. L. Ning¹, X. Zhang^{2,†}, J. S. Huang¹, B. Liu¹, M. Q. Dong¹, Zhi-Xin Guo^{1,*}

¹*State Key Laboratory for Mechanical Behavior of Materials, School of Materials Science and Engineering, Xi'an Jiaotong University, Xi'an, Shaanxi, 710049, China.*

²*Shaanxi Key Laboratory of Surface Engineering and Remanufacturing College of Mechanical and Materials Engineering Xi'an University, Xi'an 710065, China.*

[†]zhangxian1@outlook.com

^{*}zxguo08@xjtu.edu.cn

Abstract

Recent experiments have demonstrated efficient spin transfer across layers in the van der Waals heterostructure composed of WTe_2 and Fe_3GeTe_2 , signaling a potential breakthrough in developing all-van der Waals spin-orbit torque devices. However, the reasons behind the unusually high interlayer spin transparency observed, despite the weak van der Waals interactions between layers, remain unclear. In this study, we employ density functional theory and the non-equilibrium Green's function method to explore this phenomenon. We find that the efficient cross-layer spin transfer arises from direct hybridization of p-orbitals between tellurium atoms at the interface. This interlayer orbital hybridization lowers the electronic potential barrier and significantly modifies the spin-polarized electronic structure of Fe_3GeTe_2 . Consequently, an effective channel for spin-polarized transport is established between WTe_2 and Fe_3GeTe_2 , leading to high interlayer spin transparency. Combining this enhanced spin transparency with the large spin Hall angle of WTe_2 explains the high spin-orbit torque efficiency observed experimentally. Furthermore, we predict that applying a gate voltage can further increase this efficiency. Our findings offer a pathway for designing high-performance, all-van der Waals spin-orbit torque devices.

I. INTRODUCTION

Spintronics, a promising next-generation information technology, relies on the effective generation and injection of spin currents. Spin-orbit torque (SOT), induced by out-of-plane spin-polarized currents generated in materials with a high spin Hall effect (SHE) and injected into a ferromagnetic (FM) layer, has been successfully employed to efficiently manipulate magnetization, enabling the development of commercial SOT-MRAM devices [1–3]. Significant efforts have been dedicated to exploring novel materials for high-performance SOT devices [4–8]. A critical challenge in achieving efficient SOT-based spintronic devices is maximizing the SOT efficiency, defined as $\xi = \theta_{\text{SH}} \cdot T_{\text{int}}$ [9], where $\theta_{\text{SH}} = |J_s|/|J_c|$ represents the spin Hall angle, quantifying the conversion efficiency of charge current density (J_c) into spin current density (J_s). T_{int} is the spin transparency across the interface between the high-SHE material and the FM layer.

To date, various high spin-orbit coupling (SOC) materials, including heavy metals (e.g., W, Ta, Pt) [10–13], topological insulators (TIs) [14–16], and more recently, topological semimetals (TSMs) [17–20], have been extensively studied to optimize their θ_{SH} . However, investigations of T_{int} remain scarce. This is primarily because FM materials commonly used in SOT devices, such as Co, Fe, and their alloys (e.g., CoFeB), are metallic and exhibit strong interface interactions with SOC materials, which are generally assumed to result in efficient spin transparency (i.e., large T_{int}).

In parallel, rapid advancements in van der Waals (vdW) materials and their heterostructures offer new opportunities for enhancing spintronic functionalities. Recently, various two-dimensional (2D) ferromagnetic (FM) vdW materials have been discovered [21,22], including CrX_3 ($X = \text{I, Cl, and Br}$) [23–25], $\text{Cr}_2\text{Ge}_2\text{Te}_6$ [26–28], and Fe_3GeTe_2 (FGT) [29–31]. Among these, 2D FGT has garnered significant attention due to its relatively high Curie temperature ($T_c \sim 220$ K) and perpendicular magnetic anisotropy (PMA) [32,33], characteristics that make FGT a promising candidate for applications in 2D spintronic devices.

Very recently, a remarkable breakthrough in all-vdW SOT devices has been reported based on the WTe_2/FGT heterostructure [33]. This all-vdW SOT device exhibited an exceptionally high SOT efficiency ($\xi = 4.6$), which is significantly greater than that of traditional SOT devices, such as Pt/CoFeB ($\xi = 0.093$) and Ta/CoFeB ($\xi = 0.05\text{--}0.08$), as well as recently developed "half-vdW" SOT devices, including WTe_2/Py

($\xi = 0.09-0.51$), Pt/FGT ($\xi = 0.12-0.14$), and $\text{WTe}_x/\text{CoFeB}$ ($\xi = 0.426$) [34–38]. This discovery is particularly striking because the interface interaction between the FM and SOC materials is weakest in all-vdW SOT devices (vdW bonding) compared to traditional and "half-vdW" devices (chemical bonding). Typically, weaker interface interactions correlate with a smaller T_{int} and consequently lower SOT efficiency. Therefore, understanding the underlying mechanism responsible for the unusually high SOT efficiency in the WTe_2/FGT heterostructure is crucial and would provide significant guidance for the further development of high-performance all-vdW SOT devices.

In this work, we employ density functional theory (DFT) and non-equilibrium Green's function (NEGF) calculations to investigate the interfacial interaction and cross-plane electronic transport properties of the WTe_2/FGT heterostructure. Despite the weak vdW interlayer interaction, our results reveal significant p-orbital hybridization between Te atoms in WTe_2 and FGT at the interface. This pronounced interlayer orbital hybridization establishes an effective spin-polarized transport channel between the two layers. Consequently, the heterostructure exhibits an unusually large cross-plane T_{int} for spin-up electrons. Combined with the large θ_{SH} in WTe_2 , this leads to the observed high SOT efficiency.

II. METHOD

Electronic structure calculations of 1T'- WTe_2/FGT vdW heterostructure are performed within the framework of ab initio DFT using the projector-augmented wave (PAW) potentials, as implemented in Vienna Ab initio Simulation Package (VASP) [39–41]. The Perdew-Burke-Ernzerhof (PBE) exchange-correlation function is taken into account with generalized gradient approximation (GGA) to determine the exchange-correlation coupling [42]. The semiempirical dispersion-corrected DFT scheme of Grimme (DFT-D3 approximation) is applied to evaluate the weak interlayer vdW interaction [43]. The vacuum region is set to be about 15 Å in the Z-direction to address the image of charge transfer and eliminate the interaction between the periodic boundary. A plane-wave energy cutoff of 500 eV ensures total energy convergence, with an energy convergence threshold of 10^{-6} eV for both monolayers and the heterostructure. The reciprocal space is sampled by a fine grid of $14 \times 14 \times 1$, $16 \times 10 \times 1$ and $9 \times 9 \times 1$ Monkhorst-Pack k points in the Brillouin zone (BZ) for geometrical optimization for monolayer FGT, monolayer WTe_2 and their heterostructure, respectively [44]. The GGA + U method accounts for the localized 3d orbitals, with U_{eff}

selected to be 4 eV for the 3d orbitals of Fe according to previous studies. Structural relaxations are carried out until the force on each atom is less than 0.01 eV/Å. In the DFT calculations, lattice constants of $a = 3.49$ Å and $b = 6.28$ Å are used for WTe₂ [45], while $a = b = 3.99$ Å are used for FGT [46].

The quantum transport properties are calculated based on DFT combined with the Keldysh NEGF formalism, as implemented in the Atomistix ToolKit (ATK) 2019 package [47]. In the NEGF-DFT transport simulation, the physical quantities are expanded by a linear combination of atomic orbital (LCAO) basis set [48,49]. PseudoDojo pseudopotential and GGA in the form of PBE function are utilized to represent the exchange and correlation interactions [50]. The spin-resolved conductance is obtained by the Landauer-Buttiker formula:

$$G_{\sigma} = \frac{e^2}{h} \sum_{k_{\parallel}} T_{\sigma}(k_{\parallel}, E_F) \quad (1)$$

where $T_{\sigma}(k_{\parallel}, E_F)$ is the transmission coefficient with spin σ at the transverse Bloch wave vector $k_{\parallel} = (k_x, k_y)$ and the Fermi level E_F , e is the electron charge and h is the Planck constant. $11 \times 11 \times 1$ Monkhorst-Pack k -point mesh is used. The real-space mesh cut-off is set to be 120 hartree. The numerical tolerance of the Hamiltonian matrix of self-consistency is restricted to 10^{-4} .

III. RESULT AND DISCUSSION

We first present the atomic and electronic properties of monolayer WTe₂ and FGT. The monolayer WTe₂, naturally obtained via mechanical stripping, adopts a 1T' phase with spatial inversion symmetry. In this phase, spontaneous Peierls distortions cause W atoms to deviate from their ideal positions, forming a distorted octahedral structure [51]. As a result, 1T'-WTe₂ exhibits mirror symmetry only for the bc plane, but not for the ac plane (Fig. 1(a)). The projected band structure of monolayer WTe₂ is shown in Fig. 1(b) and Fig. S1(a). WTe₂ displays metallic characteristics, with energy bands near the E_F predominantly contributed by W atoms. Additionally, energy bands associated with Te atoms, characterized by strong p-d hybridization with W atoms, also appear around E_F , reflecting the shallow energy level of p orbitals in WTe₂. Figs. 1(c) and 1(d) additionally show the atomic structure and the projected band structure of monolayer FGT. As observed in Fig. 1(d), FGT also exhibits metallic behavior, with most energy bands crossing E_F contributed by the spin-down electrons of Fe atoms. Nonetheless, several energy bands from the spin-up electrons of Fe and Te atoms also cross E_F . The presence of Te-characteristic energy bands near E_F (see Fig. S1(b)) indicates the high activity of

p orbitals in Te atoms within FGT. Considering the shallow energy level of p orbitals in Te atoms of both WTe₂ and FGT, significant p-p orbital hybridization is expected between Te atoms at the interface of the heterostructure. This hybridization is stronger than the interfacial orbital hybridization typically observed in other vdW heterostructures.

Next, we discuss the WTe₂/FGT heterostructure. The in-plane lattice constants of freestanding WTe₂ and FGT are $a = 3.48 \text{ \AA}/b = 6.25 \text{ \AA}$ and $a = b = 3.99 \text{ \AA}$, respectively. A $2 \times 2/\sqrt{3}$ super-periodicity of WTe₂ is commensurate with the $\sqrt{3} \times \sqrt{3}$ FGT lattice, resulting in lattice mismatches of 0.7% and 4.2% along the a- and b-directions, respectively. As shown in Fig. S2, we consider three typical stacking configurations for the WTe₂/FGT heterostructure: hollow, bridge, and top configurations. Total-energy calculations reveal that the hollow configuration (Fig. 2(a)) is the most stable, being 2.21 meV and 140.02 meV more stable than the bridge and top configurations, respectively. Consequently, all subsequent studies are based on the hollow configuration. The minimum distance between the nearest interlayer Te atoms of WTe₂ and FGT in this configuration is 3.73 Å. Given that the atomic radius of Te is 1.37 Å, the sum of their atomic radii is significantly smaller than the interlayer spacing. This indicates that the interlayer interaction between WTe₂ and FGT is of the vdW type.

To confirm the energetic stability of the WTe₂/FGT heterostructure, we calculate the binding energy (E_b) between WTe₂ and FGT. The binding energy is defined as $E_b = (E_{\text{tot}} - E_W - E_F)/S$, where E_{tot} , E_W and E_F represent the total energy of the WTe₂/FGT heterostructure, monolayer WTe₂ and monolayer FGT, respectively. S denotes the cross-sectional area of the system. For the hollow configuration, we find $E_b = -190 \text{ meV/\AA}^2$, indicating that the heterostructure is energetically stable under vdW interlayer interactions. Notably, the binding energy of the WTe₂/FGT heterostructure is significantly larger than that of typical vdW materials, such as bilayer graphene (-19 meV/Å²) [52], h-BN (-19 meV/Å²) [53], and MoS₂ (-40 meV/Å²) [53]. This suggests that the WTe₂/FGT heterostructure may exhibit more efficient interlayer electronic transport properties compared to conventional vdW materials.

We further investigate the electronic properties of the WTe₂/FGT heterostructure. Figs. 2(c)-2(d) present the projected spin-polarized energy bands of the heterostructure. Interestingly, the projected band structures of WTe₂ and FGT in the heterostructure differ significantly from those of the freestanding monolayers. This result indicates that the weak vdW interlayer interaction induces a substantial modification of the band

structure in the WTe_2/FGT heterostructure. Additionally, we calculate the electron transfer between WTe_2 and FGT and find that only a small amount of charge (0.047 e per unit cell) transfers from FGT to WTe_2 . This observation suggests that the significant band structure variation in the heterostructure is not driven by charge transfer. Instead, it is most likely attributed to orbital hybridization between interlayer Te atoms.

The significant orbital hybridization is further verified by the projected energy bands. As shown in Fig. 2(c), there is a pronounced overlap of energy bands contributed by WTe_2 and FGT for the spin-up electrons near E_F , as highlighted by the red circles. This observation is corroborated by the calculated partial density of states (PDOS), which shows several peaks from WTe_2 and FGT aligning at the same energy levels (Fig. 2(b)). Furthermore, the element-projected band structure analysis reveals that most overlapping energy bands originate from the p_x/p_y orbitals of Te atoms at the interface (Figs. 3(a) and 3(c)). This result aligns with our earlier discussion, confirming the strong p-p orbital hybridization between the Te atoms in WTe_2 and FGT at the interface. In contrast, for spin-down electrons, the energy bands from WTe_2 and FGT exhibit minimal overlap (Fig. 2(d)). This finding is also supported by the PDOS (Fig. 2(b)), where the peaks from WTe_2 and FGT rarely align at the same energy levels. The calculated wavefunctions for the Te atoms, shown in Figs. 4(a) and 4(b), further illustrate this difference. For spin-up electrons, there is significant wavefunction overlap (primarily from p-orbitals) between interlayer Te atoms, whereas the overlap is negligible for spin-down electrons. This result is consistent with the PDOS analysis, indicating that the spin-up electronic states predominantly contribute to the interfacial electronic conductance. Moreover, the differential charge density (Fig. 4(c)) reveals a remarkable charge density redistribution in FGT, despite the limited interlayer charge transfer (0.047 e). This redistribution explains the substantial modulation of FGT's band structure in the WTe_2/FGT heterostructure.

Finally, we discuss the electronic transport properties of the WTe_2/FGT heterostructure. As shown in Fig. 4(d), the electrostatic potential barrier between WTe_2 and FGT in the heterostructure is 10.77 eV, indicating a Schottky-type interface contact. However, this barrier is significantly smaller than that of typical 2D vdW heterostructures composed of semiconductors and metals [54–56], which is attributed to the strong p-p orbital hybridization between interlayer Te atoms. A smaller potential barrier generally implies a higher electronic conductance. To further investigate the interfacial spin transport properties, we construct a 2D heterostructure device model, as

illustrated in Fig. 5(a). The calculated spin-polarized transmission is shown in Fig. 5(b), where the transmission of the spin-up state is more than an order of magnitude larger than that of the spin-down state near E_F . This result is consistent with the analysis of spin-polarized electronic structures discussed above. This finding demonstrates that the WTe_2 /FGT interface acts as an efficient spin filter. The spin current generated in WTe_2 via the SOT effect can be efficiently transferred into FGT, highlighting the potential of this heterostructure for spintronic applications.

To further evaluate the spin-transfer efficiency from WTe_2 to FGT, we additionally calculate the electronic conductance of spin-up state. The electronic conductivity of the heterostructure is found to be 2.74×10^4 S/m at the E_F . For comparison, we also examine the spin-transfer efficiency at the WTe_2 - WTe_2 and FGT-FGT interfaces. The electronic conductance is calculated using the same device model, replacing the WTe_2 /FGT heterostructure with WTe_2 / WTe_2 and FGT/FGT, respectively. As shown in Fig. 5(c), the spin-up electronic conductance of the WTe_2 /FGT heterostructure is obviously higher than that of WTe_2 / WTe_2 around the E_F , demonstrating the excellent spin-transfer properties of the WTe_2 /FGT interface. It is worth noting that the electronic conductance of both WTe_2 /FGT and WTe_2 / WTe_2 is lower than that of FGT/FGT, as FGT is a good metal with high electronic conductance. Nonetheless, the electronic conductance of WTe_2 /FGT can be substantially enhanced by tuning the energy level (chemical potential). For instance, at E_F , the conductance of WTe_2 /FGT is approximately 7.63×10^{-6} S, but it increases dramatically to 7.80×10^{-5} S when the energy level is shifted to -0.75 eV, reaching one-third of the conductance of FGT/FGT. This result suggests that by applying an appropriate gate voltage, highly efficient spin transfer can be achieved between WTe_2 and FGT flacks.

IV. CONCLUSION

In summary, based on the DFT calculations, we reveal the significant p-orbital hybridization between the interlayer Te atoms in the WTe_2 /FGT vdW heterostructure. Such orbital hybridization significantly reduces the interface electronic potential barrier and modifies the spin-polarized electronic structure of FGT, resulting in the formation of an effective spin-polarized transport channel between WTe_2 and FGT. The NEGF calculations further demonstrate a large spin-polarized transmission, yielding a spin conductivity of 2.74×10^4 S/m for spin-up electrons across the WTe_2 /FGT layers. This confirms the unusually high cross-plane spin transparency at the vdW interface. Given

the large spin Hall angle of WTe_2 , this finding naturally explains the remarkably high SOT efficiency observed in experiments. We also predict that higher SOT efficiency can be achieved through the application of gate voltage. This study provides an efficient approach to exploring and optimizing vdW heterostructures with high cross-plane spin transparency, which is particularly critical for designing high-performance all-vdW spintronic devices.

Acknowledgments

This work was supported by the Science Fund for Distinguished Young Scholars of Shaanxi Province (No. 2024JC-JCQN-09), Natural Science Foundation of China (No. 12474237), and Natural Science Foundation of Shaanxi Province (Grant No. 2023-JC-QN-0768).

Reference

- [1] L. Liu, C.-F. Pai, Y. Li, H. W. Tseng, D. C. Ralph, and R. A. Buhrman, Spin-torque switching with the giant spin Hall effect of tantalum, *Science* 336, 555 (2012).
- [2] I. M. Miron, K. Garello, G. Gaudin, P.-J. Zermatten, M. V. Costache, S. Auffret, S. Bandiera, B. Rodmacq, A. Schuhl, and P. Gambardella, Perpendicular Switching of a Single Ferromagnetic Layer Induced by In-Plane Current Injection, *Nature (London)* 476, 189 (2011).
- [3] J. Ryu, S. Lee, K. J. Lee, and B. G. Park, Current-induced spin-orbit torques for spintronic applications, *Adv. Mater.* 32, 1907148 (2020).
- [4] Y. Fan, P. Upadhyaya, X. Kou, M. Lang, S. Takei, Z. Wang, J. Tang, L. He, L.-T. Chang, M. Montazeri, G. Yu, W. Jiang, T. Nie, R. N. Schwartz, Y. Tserkovnyak, and K. L. Wang, Magnetization switching through giant spin-orbit torque in a magnetically doped topological insulator heterostructure, *Nat. Mater.* 13, 699 (2014).
- [5] H. Kurebayashi, J. Sinova, D. Fang, A. C. Irvine, T. D. Skinner, J. Wunderlich, V. Novák, R. P. Campion, B. L. Gallagher, E. K. Vehstedt, L. P. Zârbo, K. Výborný, A. J. Ferguson, and T. Jungwirth, An antidamping spin-orbit torque originating from the Berry curvature, *Nat. Nanotechnol.* 9, 211 (2014).
- [6] P.-H. Lin, B.-Y. Yang, M.-H. Tsai, P.-C. Chen, K.-F. Huang, H.-H. Lin, and C.-H. Lai,

- Manipulating exchange bias by spin-orbit torque, *Nat. Mater.* 18, 335 (2019).
- [7] C. K. Safeer, E. Jué, A. Lopez, L. Buda-Prejbeanu, S. Auffret, S. Pizzini, O. Boulle, I. M. Miron, and G. Gaudin, Spin-orbit torque magnetization switching controlled by geometry, *Nat. Nanotechnol.* 11, 143 (2016).
- [8] S. Fukami, C. Zhang, S. DuttaGupta, A. Kurenkov, and H. Ohno, Magnetization Switching by Spin-Orbit Torque in an Antiferromagnet-Ferromagnet Bilayer System, *Nat. Mater.* 15, 535 (2016).
- [9] F. Hellman, A. Hoffman, Y. Tserkovnyak, G. S. D. Beach, E. E. Fullerton, C. Leighton, A. H. MacDonald, D. C. Ralph, D. A. Arena, et al., Interface-induced phenomena in magnetism, *Rev. Mod. Phys.* 89, 025006 (2017).
- [10] C. Zhang, S. Fukami, H. Sato, F. Matsukura, and H. Ohno, Spin-orbit torque induced magnetization switching in nano-scale Ta/CoFeB/MgO, *Appl. Phys. Lett.* 107, 012401 (2015).
- [11] X. Qiu, K. Narayanapillai, Y. Wu, P. Deorani, D.-H. Yang, W.-S. Noh, J.-H. Park, K.-J. Lee, H.-W. Lee, and H. Yang, Spin-orbit torque engineering via oxygen manipulation, *Nat. Nanotechnol.* 10, 333 (2015).
- [12] C. Safranski, E. A. Montoya, and I. N. Krivorotov, Spin-orbit torque driven by a planar Hall current, *Nat. Nanotechnol.* 14, 27 (2019).
- [13] J. W. Lee, Y.-W. Oh, S.-Y. Park, A. I. Figueroa, G. van der Laan, G. Go, K.-J. Lee, and B.-G. Park, Enhanced spin-orbit torque by engineering Pt resistivity in Pt/Co/AlO_x structures, *Phys. Rev. B* 96, 064405 (2017).
- [14] J. Han, A. Richardella, S. A. Siddiqui, J. Finley, N. Samarth, and L. Liu, Room-Temperature Spin-Orbit Torque Switching Induced by a Topological Insulator, *Phys. Rev. Lett.* 119, 077702 (2017).
- [15] N. H. D. Khang, Y. Ueda, and P. N. Hai, A conductive topological insulator with large spin Hall effect for ultralow power spin-orbit torque switching, *Nat. Mater.* 17, 808 (2018).
- [16] M. DC, R. Grassi, J.-Y. Chen, M. Jamali, D. R. Hickey, D. Zhang, Z. Zhao, H. Li, P. Quarterman, Y. Lv, M. Li, A. Manchon, K. A. Mkhoyan, T. Low, and J.-P. Wang, Room-temperature high spin-orbit torque due to quantum confinement in sputtered Bi_xSe_(1-x) films, *Nat. Mater.* 17, 800 (2018).
- [17] D. MacNeill, G. M. Stiehl, M. H. D. Guimarães, N. D. Reynolds, R. A. Buhrman, and D. C. Ralph, Thickness dependence of spin-orbit torques generated by WTe₂, *Phys. Rev. B* 96, 054450 (2017).
- [18] D. MacNeill, G. M. Stiehl, M. H. D. Guimaraes, R. A. Buhrman, J. Park, and D. C. Ralph,

Control of spin–orbit torques through crystal symmetry in WTe₂/Ferromagnet bilayers, *Nat. Phys.* 13, 300 (2017).

- [19] P. Li, W. Wu, Y. Wen, C. Zhang, J. Zhang, S. Zhang, Z. Yu, S. A. Yang, A. Manchon, and X. X. Zhang, Spin-momentum locking and spin-orbit torques in magnetic nano-heterojunctions composed of Weyl semimetal WTe₂, *Nat. Commun.* 9, 3990 (2018).
- [20] B. Zhao, B. Karpiak, D. Khokhriakov, A. Johansson, A. M. Hoque, X. Xu, Y. Jiang, I. Mertig, and S. P. Dash, Unconventional charge–spin conversion in Weyl-semimetal WTe₂, *Adv. Mater.* 32, 2000818 (2020).
- [21] C. Gong, L. Li, Z. Li, H. Ji, A. Stern, Y. Xia, T. Cao, W. Bao, C. Wang, Y. Wang et al., Discovery of intrinsic ferromagnetism in two-dimensional van der Waals crystals, *Nature (London)* 546, 265 (2017).
- [22] B. Huang, G. Clark, E. Navarro-Moratalla, D. R. Klein, R. Cheng, K. L. Seyler, D. Zhong, E. Schmidgall, M. A. McGuire, D. H. Cobden et al., Layer-dependent ferromagnetism in a van der Waals crystal down to the monolayer limit, *Nature (London)* 546, 270 (2017).
- [23] S. Jiang, L. Li, Z. Wang, K. F. Mak, and J. Shan, Controlling magnetism in 2D CrI₃ by electrostatic doping, *Nat. Nanotechnol.* 13, 549 (2018).
- [24] Z. Wang, I. Gutiérrez-Lezama, N. Ubrig, M. Kroner, M. Gibertini, T. Taniguchi, K. Watanabe, A. Imamoğlu, E. Giannini, and A. F. Morpurgo, Very large tunneling magnetoresistance in layered magnetic semiconductor CrI₃, *Nat. Commun.* 9, 2516 (2018).
- [25] G. T. Lin, X. Luo, F. C. Chen, J. Yan, J. J. Gao, Y. Sun, W. Tong, P. Tong, W. J. Lu, Z. G. Sheng, W. H. Song, X. B. Zhu, and Y. P. Sun, Critical behavior of two-dimensional intrinsically ferromagnetic semiconductor CrI₃, *Appl. Phys. Lett.* 112, 072405 (2018).
- [26] Y. Sun, R. C. Xiao, G. T. Lin, R. R. Zhang, L. S. Ling, Z. W. Ma, X. Luo, W. J. Lu, Y. P. Sun, and Z. G. Sheng, Effects of hydrostatic pressure on spin-lattice coupling in two-dimensional ferromagnetic Cr₂Ge₂Te₆, *Appl. Phys. Lett.* 112, 072409 (2018).
- [27] J. Zeisner, A. Alfonsov, S. Selzer, S. Aswartham, M. P. Ghimire, M. Richter, J. van den Brink, B. Buchner, and V. Kataev, Magnetic anisotropy and spin-polarized two-dimensional electron gas in the van der Waals ferromagnet Cr₂Ge₂Te₆, *Phys. Rev. B* 99, 165109 (2019).
- [28] M. Suzuki, B. Gao, K. Koshiishi, S. Nakata, K. Hagiwara, C. Lin, Y. X. Wan, H. Kumigashira, K. Ono, S. Kang, S. Kang, J. Yu, M. Kobayashi, S. W. Cheong, and A. Fujimori, Coulomb-interaction effect on the two-dimensional electronic structure of the van der Waals ferromagnet Cr₂Ge₂Te₆, *Phys. Rev. B* 99, 161401(R) (2019).
- [29] K. Kim, J. Seo, E. Lee, K. T. Ko, B. S. Kim, B. G. Jang, J. M. Ok, J. Lee, Y. J. Jo, W. Kang,

- J. H. Shim, C. Kim, H. W. Yeom, B. Il Min, B. J. Yang, and J. S. Kim, Large anomalous Hall current induced by topological nodal lines in a ferromagnetic van der Waals semimetal, *Nat. Mater.* 17, 794 (2018).
- [30] Z. Fei, B. Huang, P. Malinowski, W. Wang, T. Song, J. Sanchez, W. Yao, D. Xiao, X. Zhu, A. F. May, W. Wu, D. H. Cobden, J. H. Chu, and X. Xu, Two-dimensional itinerant ferromagnetism in atomically thin Fe_3GeTe_2 , *Nat. Mater.* 17, 778 (2018).
- [31] Y. Deng, Y. Yu, Y. Song, J. Zhang, N. Z. Wang, Z. Sun, Y. Yi, Y. Z. Wu, S. Wu, J. Zhu, J. Wang, X. H. Chen, and Y. Zhang, Gate-tunable room-temperature ferromagnetism in two-dimensional Fe_3GeTe_2 , *Nature (London)* 563, 94 (2018).
- [32] H.-J. Deiseroth, K. Aleksandrov, C. Reiner, L. Kienle, and R. K. Kremer, Fe_3GeTe_2 and Ni_3GeTe_2 —two new layered transition-metal compounds: crystal structures, HRTEM investigations, and magnetic and electrical properties, *Eur. J. Inorg. Chem.* 2006, 1561 (2006).
- [33] I. Shin, W. J. Cho, E. S. An, S. Park, H. W. Jeong, S. Jang, W. J. Baek, S. Y. Park, D. H. Yang, J. H. Seo, G. Y. Kim, M. N. Ali, S. Y. Choi, H. W. Lee, J. S. Kim, S. D. Kim, and G. H. Lee, Spin-orbit torque switching in an all-van der Waals heterostructure, *Adv. Mater.* 34, 2101730 (2022).
- [34] S. Hori, K. Ueda, T. Kida, M. Hagiwara, and J. Matsuno, Spin-orbit torque generation in bilayers composed of CoFeB and epitaxial SrIrO_3 grown on an orthorhombic DyScO_3 substrate, *Appl. Phys. Lett.* 121, 022402 (2022).
- [35] Y. Zheng, T. Wang, X. Su, Y. Chen, Y. Wang, H. Lv, S. Cardoso, D. Yang, and J. Cao, Enhancement of spin-orbit torques in $\text{Ta}/\text{Co}_{20}\text{Fe}_{60}\text{B}_{20}/\text{MgO}$ structures induced by annealing, *AIP Advances.* 7, 075305 (2017).
- [36] S. Shi, S. Liang, Z. Zhu, K. Cai, S. D. Pollard, Y. Wang, J. Wang, Q. Wang, P. He, J. Yu, G. Eda, G. Liang, and H. Yang, All-electric magnetization switching and Dzyaloshinskii-Moriya interaction in WTe_2 /ferromagnet heterostructures, *Nat. Nanotechnol.* 14, 945 (2019).
- [37] X. Wang, J. Tang, X. Xia, C. He, J. Zhang, Y. Liu, C. Wan, C. Fang, C. Guo, W. Yang, Y. Guang, X. Zhang, H. Xu, J. Wei, M. Liao, X. Lu, J. Feng, X. Li, Y. Peng, H. Weil, R. Yang, D. Shi, X. Zhang, Z. Han, Z. Zhang, G. Zhang, G. Yu, and X. Han, Highly Efficient Spin-Orbit Torque and Switching of Layered Ferromagnet Fe_3GeTe_2 , *Sci. Adv.* 5, eaaw8904 (2019).
- [38] X. Li, P. Li, V. D. H. Hou, M. DC, C.-H. Nien, F. Xue, D. Yi, C. Bi, C.-M. Lee, S.-J. Lin, W. Tsai, Y. Suzuki, and S. X. Wang, Large and robust charge-to-spin conversion in

- sputtered conductive WTe_x with disorder, *Matter* 4, 1639 (2021).
- [39] G. Kresse and J. Furthmüller, Efficient iterative schemes for ab initio total-energy calculations using a plane-wave basis set, *Phys. Rev. B* 54, 11169 (1996).
- [40] P. E. Blöchl, Projector augmented-wave method, *Phys. Rev. B* 50, 17953 (1994).
- [41] G. Kresse and J. Hafner, Ab initio molecular dynamics for liquid metals, *Phys. Rev. B* 47, 558 (1993).
- [42] J. P. Perdew, K. Burke, and M. Ernzerhof, Generalized Gradient Approximation Made Simple, *Phys. Rev. Lett.* 77, 3865 (1996).
- [43] S. Grimme, Semiempirical GGA-type density functional constructed with a long-range dispersion correction, *J. Comput. Chem.* 27, 1787 (2006).
- [44] H. J. Monkhorst and J. D. Pack, Special points for Brillouin-zone integrations, *Phys. Rev. B* 13, 5188 (1976).
- [45] E. J. Sie, C. M. Nyby, C. D. Pemmaraju, S. J. Park, X. Shen, J. Yang, M. C. Hoffmann, B. K. Ofori-Okai, R. Li, A. H. Reid, S. Weathersby, E. Mannebach, N. Finney, D. Rhodes, D. Chenet, A. Antony, L. Balicas, J. Hone, T. P. Devereaux, T. F. Heinz, X. Wang and A. M. Lindenberg, An ultrafast symmetry switch in a Weyl semimetal, *Nature (London)* 565, 61 (2019).
- [46] H.-J. Deiseroth, K. Aleksandrov, C. Reiner, L. Kienle, and R. K. Kremer, Fe_3GeTe_2 and Ni_3GeTe_2 —Two New Layered Transition-Metal Compounds: Crystal Structures, HRTEM Investigations, and Magnetic and Electrical Properties, *Eur. J. Inorg. Chem.* 2006, 1561 (2006).
- [47] M. Brandbyge, J.-L. Mozos, P. Ordejón, J. Taylor, and K. Stokbro, Density-functional method for nonequilibrium electron transport, *Phys. Rev. B* 65, 165401 (2002).
- [48] J. S. Huang, P. Li, X. X. Ren, and Z.-X. Guo, Promising properties of a sub-5-nm monolayer $MoSi_2N_4$ transistor, *Phys. Rev. Appl.* 16, 044022 (2021).
- [49] X. Zhang, B. Liu, J. S. Huang, X. W. Cao, Y. Z. Zhang, and Z.-X. Guo, Nonvolatile spin field effect transistor based on VSi_2N_4/Sc_2CO_2 heterostructure, *Phys. Rev. B* 109, 205105 (2024).
- [50] J. P. Perdew, K. Burke, and M. Ernzerhof, Generalized Gradient Approximation Made Simple, *Phys. Rev. Lett.* 77, 3865 (1996).
- [51] F. Ye, J. Lee, J. Hu, Z. Mao, J. Wei, and P. X.-L. Feng, Environmental instability and degradation of single- and few-layer WTe_2 nanosheets in ambient conditions, *Small* 12, 5802 (2016).
- [52] K. V. Zakharchenko, J. H. Los, M. I. Katsnelson, and A. Fasolino, Atomistic simulations

of structural and thermodynamic properties of bilayer graphene, *Phys. Rev. B* 81, 235439 (2010).

- [53] H. Rydberg, M. Dion, N. Jacobson, E. Schroder, P. Hyldgaard, S. I. Simak, D. C. Langreth, and B. I. Lundqvist, Van der Waals Density Functional for Layered Structures, *Phys. Rev. Lett.* 91, 126402 (2003).
- [54] T. V. Vu, T. P. Dao, M. Idrees, H. V. Phuc, N. N. Hieu, N. T. Binh, H. B. Dinh, B. Amin, and C. V. Nguyen, Effects of different surface functionalization on the electronic properties and contact types of graphene/functionalized-GeC van der Waals heterostructures, *Phys. Chem. Chem. Phys.* 22, 7952 (2020).
- [55] X. Zhang, L. Feng, S. Zhong, Y. Ye, H. Pan, P. Liu, X. Zheng, H. Li, M. Qu, and X. Wang, Schottky barrier heights and mechanism of charge transfer at metal-Bi₂OS₂ interfaces, *Sci. China Mater.* 66, 811 (2023).
- [56] L. Cao, X. Deng, Z. Tang, R. Tan and Y. S. Ang, Designing CMOS compatible efficient ohmic contacts to WSi₂N₄ via surface-engineered Mo₂B monolayer electrodes, *J. Mater. Chem. C* 12, 648 (2024).

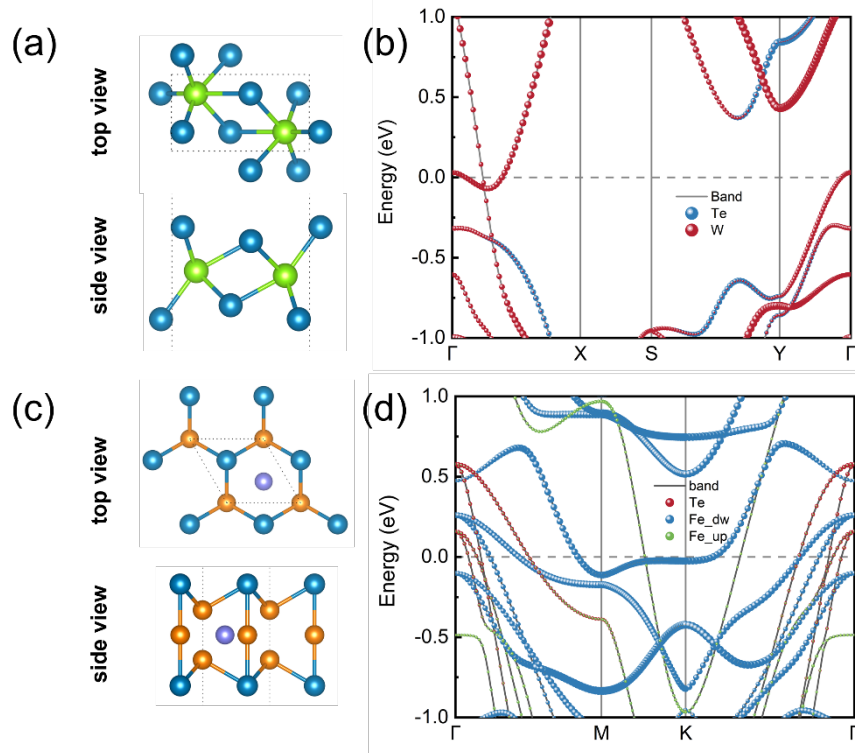


FIG.1. The atomic structures and elemental-projected energy band structures of monolayer WTe₂ (a-b) and monolayer FGT (c-d), respectively, based on DFT calculations.

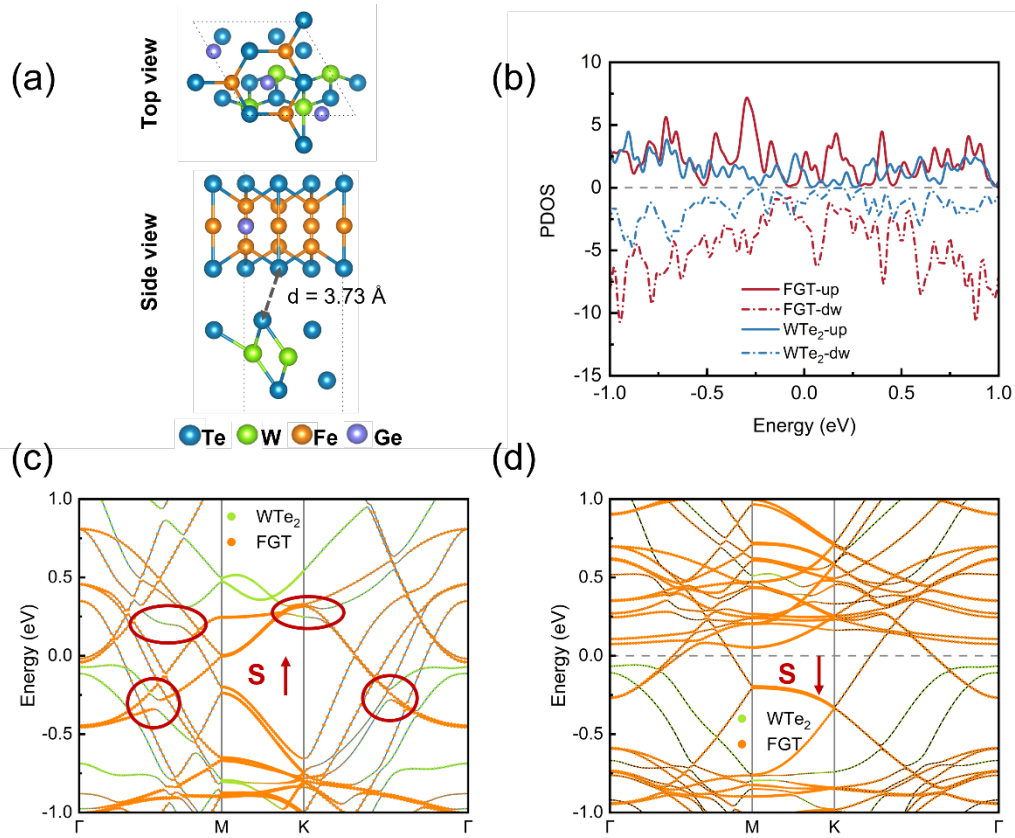


FIG.2. (a) Crystal structural of WTe₂/FGT heterostructure. Bule, green, orange and purple balls represent Te, W, Fe, Ge atoms, respectively, (b) Partial density of states of heterostructure, (c-d) Spin-up and spin-down projected electronic band structures, respectively. Green and orange points represent the contributions of WTe₂ and FGT, respectively. The red arrows represent the direction of spin polarization. Red circles indicate band hybridization.

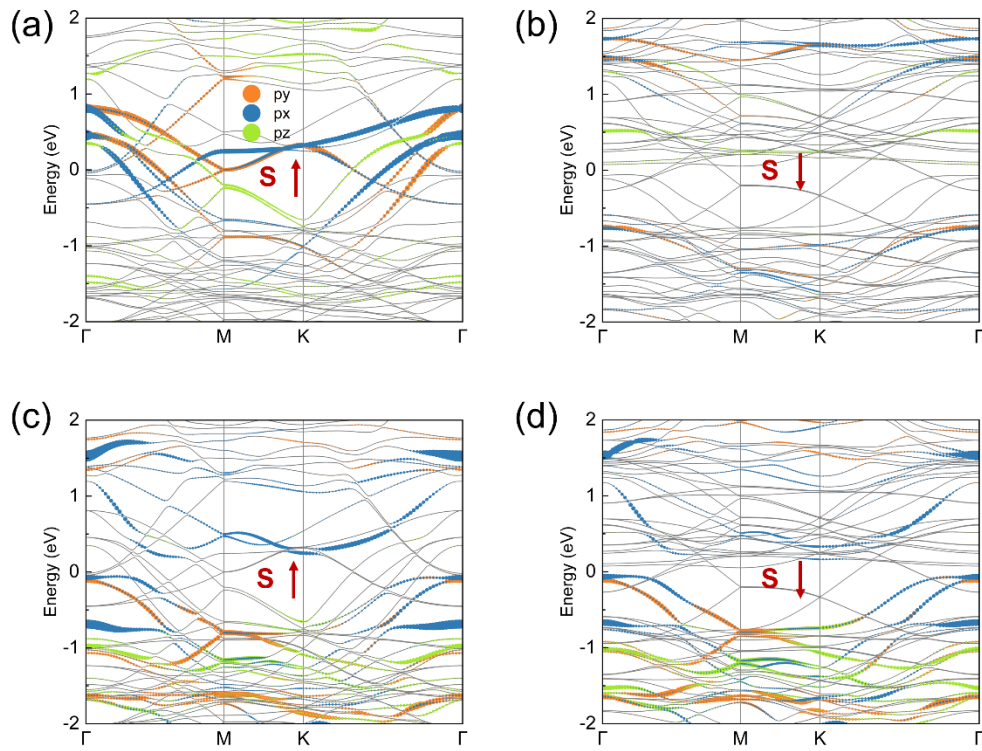


FIG.3. Orbital projection band structures of interfacial Te atoms in FGT (a-b) and WTe_2 (c-d), respectively. Orange, blue and green dots represent p_y , p_x , p_z orbitals, respectively. The red arrows represent spin polarization directions.

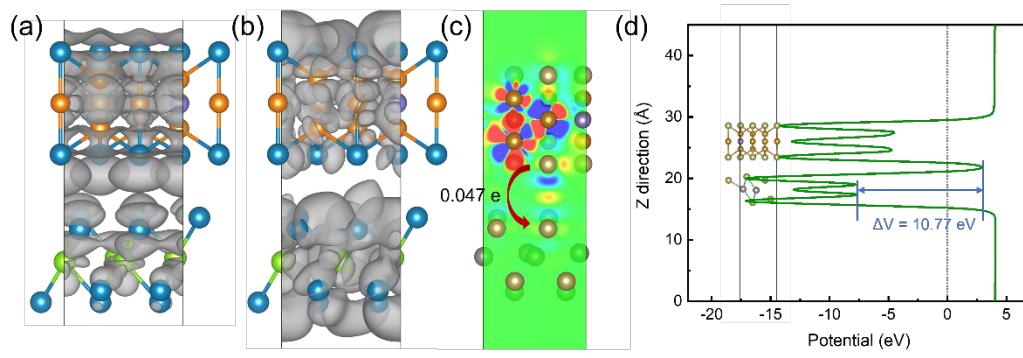


FIG.4. (a-b) Visualize the squared wave-function of the spin-up (a) and spin-down (b) components of the interfacial bonding states, respectively. An isosurface value of 4×10^{-12} e/Bohr³ is used. (c) Differential charge density in (010) surface. (d) Electrostatic potential of WTe₂/FGT heterostructure along Z direction.

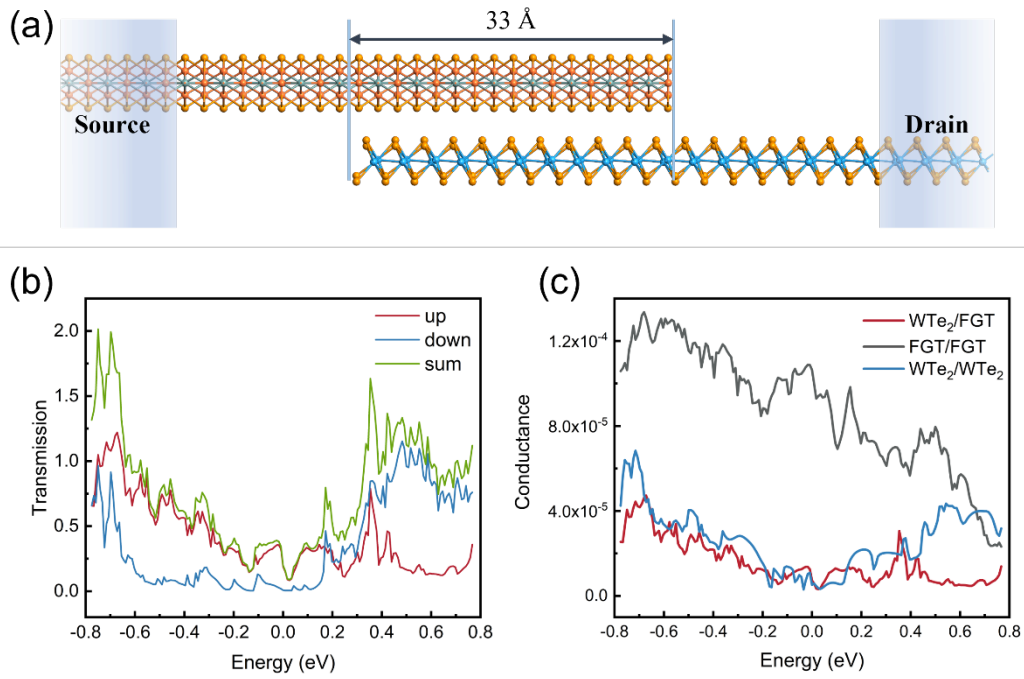


FIG.5. (a) Device structure of WTe_2/FGT heterostructure. The overlapping region in the middle is about 33 \AA . (b) The spin-dependent transmission spectrum of WTe_2/FGT device at zero bias. (c) Device spin-up conductance. Red, black, and blue lines represent WTe_2/FGT device, FGT/FGT device and $\text{WTe}_2/\text{WTe}_2$ device, respectively.